

Multiobjective optimization for scattering mitigation and scattering screen reconstruction in VLBI observations of the Galactic Center

Alejandro Mus^{1,2}, Teresa Toscano³, Hendrik Müller^{4,5}, Guang-Yao Zhao^{5,3}, Andrei Lobanov⁵, and Ciriaco Goddi^{1,6}

¹ Dipartimento di Fisica, Università degli Studi di Cagliari, SP Monserrato-Sestu km 0.7, I-09042 Monserrato, Ital
e-mail: alejandro.musmejias@unica.it

² INAF-Istituto di Radioastronomia, Via P. Gobetti 101, I-40129 Bologna, Italy

³ Instituto de Astrofísica de Andalucía CSIC, Apartado 3004, 18080 Granada, Spain

⁴ Jansky Fellow of National Radio Astronomy Observatory, 1011 Lopezville Rd, Socorro, NM 87801, USA

⁵ Max-Planck-Institut für Radioastronomie, Auf dem Hügel 69, D-53121 Bonn (Endenich), Germany

⁶ Instituto de Astronomia, Geofísica e Ciências Atmosféricas, Universidade de São Paulo, R. do Matão, 1226, São Paulo, SP 05508-090, Brazil

Received / Accepted

ABSTRACT

Context. Imaging reconstruction of interferometric data is a hard ill-posed inverse problem. Its difficulty is increased when observing the Galactic Center, which is obscured by a scattering screen. This is because the scattering breaks the one-to-one correspondence between images and visibilities.

Aims. Solving the scattering problem is one of the biggest challenges in radio imaging of the Galactic Center. In this work we present a novel strategy to mitigate its effect and constrain the screen itself using multiobjective optimization.

Methods. We exploit the potential of evolutionary algorithms to describe the optimization landscape to recover the intrinsic source structure and the scattering screen affecting the data.

Results. We successfully recover both the screen and the source in a wide range of simulated cases, including the speed of a moving screen at 230 GHz. Particularly, we can recover a ring structure in scattered data at 86 GHz.

Conclusions. Our analysis demonstrates the huge potential that recent advancements in imaging and optimization algorithms offer to recover image structures, even in weakly constrained and degenerated, possibly multi-modal settings. The successful reconstruction of the scattering screen opens the window to event horizon scale works on the Galactic Center at 86 GHz up to 116 GHz, and the study of the scattering screen itself.

Key words. Techniques: interferometric - Techniques: image processing - Techniques: high angular resolution - Methods: numerical - Galaxies: jets - Galaxies: nuclei

1. Introduction

Supermassive black holes (SMBH) are found, or expected, in the center of most galaxies (Richstone et al. 1998). The accretion of matter onto the central object is responsible for regularly observed periods of activity with a significant impact on the intergalactic and circumgalactic environments, and the evolution of their host galaxy. Additionally, SMBHs are used as a laboratory to study the physics of gravity itself. In this context, a primary laboratory is the SMBH in our own Galaxy, Sagittarius A*, or Sgr A* (Goddi et al. 2017).

Sgr A* is one of the key targets of the Event Horizon Telescope (EHT), a worldwide network of radiotelescopes that employs Very Long Baseline Interferometry (VLBI) at mm and submm wavelengths (Event Horizon Telescope Collaboration et al. 2019a; Raymond et al. 2024). The unprecedented angular resolution achieved by the EHT enabled to capture the first images of SMBHs, the one at the center of the giant elliptical galaxy M87 (Event Horizon Telescope Collaboration et al. 2019b,a,c,d,e,f, 2023)

and the one at the center of our own galaxy, in both total intensity (Event Horizon Telescope Collaboration et al. 2022a,b,c,d,e,f) and polarized light (Event Horizon Telescope Collaboration et al. 2021a,b, 2024a,b). In both targets, EHT observations reveal a ring-like feature, which is interpreted as the theoretically-predicted signature of the black hole shadow. In the case of M87*, a similar ring-like feature has subsequently also been detected with the Global Millimeter VLBI Array (GMVA) at 86 GHz (Lu et al. 2023; Kim et al. 2024a). Multi-frequency observations of the innermost regions surrounding the central SMBH are crucial to characterize the physical conditions of the accreting plasma and to constrain black hole accretion models (Mościbrodzka et al. 2014, 2016).

However, such a multi-frequency analysis remains limited for Sgr A* due to an additional effect: interstellar scattering. Interstellar scattering, caused by variations in electron density along the line-of-sight to the target, results in multipath propagation, which broadens radio images and pulse profiles of objects located in or behind the Galactic

plane. In certain directions, the scattering is significantly stronger than what is predicted by the large-scale Galactic electron distribution models (Taylor & Cordes 1993; Cordes & Lazio 2002). This pronounced scattering has long been linked to galactic HII regions and supernova remnants (SNRs) (Litvak 1971; Little 1973). Being situated at the center of our Galaxy, Sgr A* is chiefly affected by intense scattering. The size of its radio image increases with λ^2 (e.g. Bower et al. 2004; Issaoun et al. 2019), consistent with predictions for a “thin” scattering screen (Blandford & Narayan 1985).

The interferometric phase information is strongly affected by the presence of scattering. As a consequence, scattering-induced distortions on the observed data can significantly degrade the quality of the images, particularly at frequencies below 86 GHz. In this line, several strategies have been developed to mitigate the scattering effects and improve the quality and robustness of the image (Fish et al. 2014; Johnson 2016; Kouroshnia et al. 2025). These algorithms characterize the scattering kernel and incorporate a functional within the imaging deconvolution process to correct for the associated distortions. First, Fish et al. (2014) proposes to apply a Wiener filter (Wiener 1949) to the scattering kernel to increase the signal-to-noise ratio. In contrast, Johnson (2016) proposes to find the source and screen discrete reconstructions that best fit the data. As a byproduct, this algorithm is able to recover an image of both the scattering corrected observed source and an approximation of the scattering screen. The latter holds significant astrophysical information on its own and supports efforts to detect transient phenomena towards the Galactic center (Caleb et al. 2022; Beniamini et al. 2023). One of the main challenges in this context is the potential degeneracy between the scattering screen and the image. This led to the development of imaging algorithms based on multi-modal image posteriors. In particular, we base our analysis on the multiobjective evolution proposed in Müller et al. (2023) and extended in Mus et al. (2024b,a).

This manuscript presents the design, implementation, and testing of novel algorithms to mitigate the impact of (potentially dynamic) scattering screens affecting VLBI observations, by recovering both the intrinsic black hole structure images at lower frequencies and the screen itself.

Compared to traditional noise-inflation and deblurring techniques, such as those used in Event Horizon Telescope Collaboration et al. (2022c, 2024a), or even standard unimodal exploration Johnson (2016), our novel strategy effectively explores the family of local solutions—an essential feature for addressing the highly non-linear and ill-posed problem of VLBI imaging and screen modeling. Unlike methods constrained to a specific screen model (and thus a fixed intrinsic source structure), the flexibility of our approach provides a mathematically rigorous solution to the modeling and mitigation problem.

This paper is structured as follows. We present the background theory on VLBI imaging, and scattering theory in Sec. 2. In Sec. 3, we discuss the problem modelization and imaging algorithm, and verify the reconstruction with a static and dynamic screen and a static source in Sec. 4. In Sec. 5, we discuss the potential to recover the scattering screen and the black hole shadow after proper de-scattering at 86 GHz. We show the marginal distributions of the scattering screen regularizers in Sec. 6, and finally discuss future prospects in Sec. 7.

2. VLBI and imaging background

2.1. VLBI

In a VLBI array, multiple antennas observe the same source at the same time and afterwards the recorded signals get correlated. These correlated signals from the antennas (visibilities) are approximately the Fourier transform of the true sky brightness distribution at a spatial frequency determined by the baseline separating the antennas in an antenna-pair projected on the sky-plane. In particular, the visibility function $\mathcal{V}(u, v)$, representing the correlated signal between an antenna pair, is governed by the van Cittert-Zernike theorem (Thompson et al. 2017):

$$\mathcal{V}(u, v) = \iint I(l, m) e^{-2\pi i(lu + mv)} dl dm. \quad (1)$$

This equation expresses that the true sky brightness distribution, $I(l, m)$, and the observed visibilities are related as a Fourier pair. Here, (u, v) coordinates are defined by the relative baselines between antennas in the plane of the sky. However, it is crucial to recognize that, in practical scenarios, the Fourier domain is not fully sampled, leading to sparse coverage in the (u, v) -plane, particularly in VLBI contexts. This incomplete sampling makes the process of reconstructing the sky brightness distribution from the observed visibilities an ill-posed inverse problem. Additionally, these visibilities are subject to calibration errors and thermal noise. To mitigate these challenges, it is essential to account for calibration effects. Direction-independent calibration errors are modeled through station-based gain factors, g_i . The observed visibilities at a given time t for an antenna pair i, j are thus expressed as

$$V(i, j, t) = g_{i,t} g_{j,t}^* \mathcal{V}(i, j, t) + N(i, j, t), \quad (2)$$

where g_i and g_j are the station-based gains, and $N(i, j, t)$ represents the random noise associated with the baseline.

These difficulties are exasperated in sparse VLBI networks like the EHT, which, additionally, operates at high radio frequencies, rendering the data calibration and imaging processes particularly challenging. All these difficulties have required the development of a wide range of novel algorithms for image reconstruction that we describe in detail in the next subsection.

2.2. Outline of Imaging

The imaging algorithms employed in the EHT can be roughly categorized into five groups: techniques based on Bayesian exploration (Broderick et al. 2020; Tiede 2022), the regularized maximum likelihood technique (RML) (Akiyama et al. 2017b,a; Chael et al. 2018), global search techniques by multiobjective evolution (Müller et al. 2023; Mus et al. 2024a), compressive sensing (Müller & Lobanov 2022, 2023a), and inverse modeling with novel developments, e.g. by Müller & Lobanov (2023b). The majority of these algorithms achieves a moderate degree of super-resolution, i.e. robustly recover structures smaller than the original CLEAN (Högbom 1974; Clark 1980; Cornwell 2008) resolution limit. This has proven to be crucial for a reliable reconstruction of structures at the spatial scales of the event horizon.

The RML method is one of the most often used imaging techniques in the EHT (Event Horizon Telescope Collaboration et al. 2019d, 2021a, 2022c, 2023, 2024c,a). Multiple data fidelity terms and regularization terms are balanced against each other by a relative weighting. Then this weighted sum is minimized. The solution of this optimization problem is the model better described by the data. The data term takes into account how well one solution is described by the data. Often used data terms include χ^2 metrics to observed data products, e.g. the visibilities or closure products. The regularization terms, in turn, describe the plausibility of the recovered solution. Standard choices include the total variation (promoting piece wise smooth functions), total squared variation (promoting smoothness), the l1-norm (promoting sparsity), the l2-norm (reducing the overfitting) or an entropy functional.

It is crucial to use the correct relative weighting of the data and regularization terms for RML methods. The EHT has applied a strategy of thorough surveying a sufficient subset of possible parameter combinations. Multiobjective optimization aims at presenting a different strategy. The concept of optimality of a weighted sum of objectives is replaced by the concept of Pareto optimality in a multi-objective problem formulation: A solution is called Pareto optimal if the further optimization of one objective (e.g. the data term) automatically has to worsen the scoring in another one (e.g. in a regularization term). The set of all Pareto-optimal solutions is referred to as the Pareto front.

MOEA/D is an algorithm based on the genetic evolution that approximates the Pareto front (Zhang & Li 2007; Li & Zhang 2009). It has been adapted for VLBI objectives by Müller et al. (2023), where they also showed that the Pareto front in VLBI experiments has a special structure: it is separated into multiple clusters, which are interpreted as locally optimal modes of the potentially multimodal imaging problem. Furthermore, the cluster with the best solution has been found to be in practice the one closest to the ideal point (see Müller et al. 2023, for more details on this construction). This algorithm is in active use for the imaging in extremely-weak constrained settings, or problems in which internal degeneracy may cause a multimodal posterior. This includes the reconstruction of the polarization structure from the closure traces (Müller 2024), or the imaging of solar flares with the STIX instrument (Müller et al. 2024).

MO-PSO is a much faster and more accurate variant of MOEA/D that was proposed by Mus et al. (2024a). Rather than reconstructing the full image structure by an evolutionary algorithm, we just navigate the Pareto front by an evolutionary algorithm (particle swarm optimization), and solve the scaled problems by fast L-BFGS-B minimization. The Pareto front is searched over in order to minimize the distance of a Pareto-optimal solution to the ideal point. Thus, instead of recovering the full Pareto front, MO-PSO gives directly its final best image reconstruction, spending less time and computational resources.

2.3. Scattering

In this section we give an overview on the theory and motivation behind the thin-screen scattering, focused on the relevant aspects related with the goals of our strategy. For further details, we forward the interested reader to the re-

views (Rickett 1990; Narayan 1992; Johnson & Gwinn 2015; Thompson et al. 2017).

When an source is observed through a medium with spatial variations in its refractive index, it becomes distorted. Refractive inhomogeneities cause different regions of an image associated to the source to be steered and focused differently, while maintaining surface brightness (Born & Wolf 1980). In particular, radio-wave scattering in the ionized interstellar medium (ISM) is due to density inhomogeneities, as the refractivity in a plasma is approximately proportional to the local electron density (Jonson 1999).

In general, scattering is often described as resulting from turbulent media localized to a single thin screen between the source and observer (see Bower et al. 2014; Dexter et al. 2017; Psaltis et al. 2018, for instance). Through this paper, we work under the assumptions of one unique thin screen that can be approximated by n layers, although the number of screens in the line-of-sight is still an opened question (e.g. Dexter et al. 2017).

If r is a two-dimensional transverse coordinate on the screen, this screen introduces a stochastic, position-dependent phase shift $\phi(r)$ to the incoming radiation, without altering the amplitude of the waves.

Assuming the screen follows a homogeneous Gaussian distribution, the scattering can be quantified in two complementary ways: by the structure function of the phase fluctuations, $D_\phi(r) = \langle [\phi(r+r') - \phi(r')]^2 \rangle$, or by the power spectrum of the phase fluctuations, $P_\phi(q) \propto |q|^{-(\alpha+2)}$, α assumed to be 1.38¹ in this work. These approaches are related by a Fourier transform: $P_\phi(q) \propto q^2 D_\phi(q)$, with a prefactor making $P_\phi(q)$ dimensionless and independent of the observing wavelength (λ).

Diffractive and refractive scattering effects on images can be treated as distinct phenomena (Blandford & Narayan 1985). Diffractive effects, which dominate at small scales (approximately r_0), are well approximated by their ensemble-average—that is, the expectation value of the measured complex visibilities when averaging over many realizations of the scattered phases (Narayan & Goodman 1989; Goodman & Narayan 1989). This averaging effectively blurs the intrinsic image with a kernel $G(r)$ (the seeing disk). This kernel is most naturally expressed in the visibility domain as $\tilde{G}(\mathbf{b}) = e^{-\frac{1}{2}D_\phi(\mathbf{b})}$, where \mathbf{b} corresponds to the physical length of an interferometric baseline. Refractive effects can be modeled using a geometrical optics framework, where gradients of the large-scale refractive modes of the phase screen steer and focus the ensemble-average image.

The single-epoch scattered image $I_a(r)$ is related to the unscattered image $I_{\text{src}}(r)$ via Johnson & Narayan (2016); Johnson (2016):

$$I_a(r) = I_{\text{src}}(r) * G(r) + (\nabla \phi_r(r)) \cdot [I_{\text{src}}(r) * \nabla G(r)].$$

In these expressions, ∇ represents the two-dimensional transverse gradient on the phase screen. The term $I_{\text{src}}(r) * G(r)$, where $*$ denotes spatial convolution, represents the blurring effect due to scattering and is referred to as the ensemble-average image, $I_{\text{ea}}(r) = I_{\text{src}}(r) * G(r)$. The second term, $(\nabla \phi_r(r)) \cdot [I_{\text{src}}(r) * \nabla G(r)]$, accounts for additional distortions introduced by variations in the phase screen.

¹ We use the default value, 1.38, of `StochasticOptics` (Johnson 2016)

This term captures the influence of the turbulent phase gradient across the scattering screen, further modulating the observed image through spatially dependent distortions.

For each image, r is a transverse coordinate at the distance of the scattering screen D (not the distance of the source $D + R$), so the corresponding angular scales are $\theta = \frac{r}{D}$. For simplicity, throughout the remainder of this paper, we will use $\phi(r)$ to denote the refractive phase screen $\phi_r(r)$. We will denote the forward operator applying the scattering with Φ for the remainder of this manuscript, i.e.:

$$\Phi : [I_{\text{src}}, \phi] \mapsto I_a. \quad (3)$$

The Strehl ratio, $0 < S \leq 1$, is a metric commonly used in the optical literature to quantify image degradation due to scattering. It is defined as the ratio of the peak intensity of the measured point-spread function (PSF), which includes the effects of scattering, to the peak intensity of the ideal, diffraction-limited PSF, which assumes no scattering.

This concept was extended to radio interferometry by (Johnson 2016), and is defined as

$$S \simeq \frac{\theta_{uv}}{\sqrt{\theta_{uv}^2 + \theta_{\text{scatt}}^2}},$$

being θ_{uv} the full width at half maximum (FWHM) of the beam of the array and θ_{scatt} is the FWHM of I_a . Johnson (2016) Fig. 1 shows the expected S for the different arrays.

3. Problem statement

In this section, we introduce the mathematical optimization formulation utilized to model the imaging problem, along with the strategy employed. We have adopted a multiobjective optimization approach as presented in Mus et al. (2024a). For the sake of simplicity, we refer to the aforementioned paper for the mathematical formulation of the regularizers.

3.1. Modeling

Given a vector functional, $F := (f_1, \dots, f_n)$ and an image vector x , the multiobjective optimization problem (MOP) is

Problem 1 (MOP).

$$\begin{aligned} \min_{x \in D} \quad & F := (f_1(x), \dots, f_n(x)), \\ \text{subject to} \quad & \mathbf{x} \in \mathbf{F} \subseteq \mathbb{R}_{+\infty}^p, \end{aligned} \quad (\text{MOP})$$

Following the strategy presented in Müller et al. (2023); Mus et al. (2024b,a), we solve (MOP) by scalarization, i.e., by rewriting the problem as the unconstrained minimization problem

Problem 2 (MOP scalarized).

$$\begin{aligned} \min_{\mathbf{x} \in \mathbf{F} \subseteq \mathbb{R}_{+\infty}^p} \quad & F := \sum_{i=1}^n \alpha_i f_i(x), \quad \alpha_i \geq 0, \forall i = 1, \dots, n. \end{aligned} \quad (\text{MOP Scalar})$$

In this work, we recover the images by utilizing a wavelet dictionary Ψ , i.e. we model the total intensity by $I = \Psi\omega_I$,

see Sec. 3.2 for more details. Hence, for the dynamic reconstruction of a movie in full polarization and a movie of the scattering screen, we recover the following quantities at every frame:

1. The wavelet coefficients describing the image in total intensity ω_I . They are related to the image at every frame by the relation $I = \Psi\omega_I$.
2. The phase screen ϕ .

A movie is represented by a sequence of single, individual images. Hence, in the problem description MOP x is the vector:

$$x = [\omega_I, \phi^1, \phi^2, \phi^3, \dots], \quad (4)$$

where the superscript denotes the index of the frame in the movie.

The individual functionals are:

$$f_1 := R_{l1}(\Psi\omega_I), \quad (5)$$

$$f_2 := R_{tv}(\Psi\omega_I), \quad (6)$$

$$f_3 := R_{tsv}(\Psi\omega_I), \quad (7)$$

$$f_4 := R_{l2}(\Psi\omega_I), \quad (8)$$

$$f_5 := R_{flux}(\Psi\omega_I), \quad (9)$$

$$f_6 := R_{entr}(\Psi\omega_I), \quad (10)$$

$$f_7 := \sum_{j \in \text{frames}} R_{SO}(\phi^j), \quad (11)$$

$$\begin{aligned} f_8 := & \sum_{j \in \text{frames}} S_{vis}(\Phi(\Psi\omega_I, \phi^j)) + S_{amp}(\Phi(\Psi\omega_I, \phi^j)) \\ & + S_{clp}(\Phi(\Psi\omega_I, \phi^j)) + S_{cla}(\Phi(\Psi\omega_I, \phi^j)). \end{aligned} \quad (12)$$

Here, f_1 to f_6 are the standard static imaging regularizers. For their exact form we refer back to Müller et al. (2023). f_7 the Stochastic Optics functional (Johnson 2016). and f_8 the data functional. These are χ^2 of the visibilities, amplitudes, closure phases and closure amplitudes in total intensity. The data fidelity terms are evaluated on the scattered movies, while the single regularizers are evaluated on the unscattered guess solutions.

By solving Prob. (MOP) via Prob. (MOP Scalar), we obtain the (static/dynamic) reconstruction that, along with its associated power spectrum, provides the best fit to the data. In Sect. 4.1, we provide a detailed modelization of the power spectrum.

3.2. Pipeline

The pipeline used for the reconstruction employs nature-based optimization strategies: MOEA/D (Müller et al. 2023; Mus et al. 2024b) and MO-PSO (Mus et al. 2024a). The core concept of these strategies involves scalarizing the objective vector F and iteratively solving a series of subproblems. Both approaches offer significant advantages, which are discussed throughout this manuscript. For a more in-depth understanding, interested readers can refer to the cited references.

MOEA/D

To explore the Pareto front reconstructions, the interferometric reconstruction problem is modeled by

$$\tilde{f}_i = f_i + f_8$$

being f_i the ones defined from Eq. (5) to Eq. (11) and f_8 the corresponding data term functional associated to the problem.

With this formulation, every functional \tilde{f}_i gives a set of solutions that fit the data and are affected only by the regularizer f_i .

To solve the full MO, a genetic algorithm is applied. That is to say, first, the multidimensional space of functions is gridded, and a random sample of individuals (in our case images or movies) is drawn. Then, a mutation and cross-over operation is applied over the individuals producing new populations (Müller et al. 2023).

MO-PSO

For every subproblem, we apply MO-PSO (for instance Du & Swamy 2016), considering a swarm composed by the hyperparameters α_i appearing in Prob. (MOP Scalar) acting on every regularizer. In this way, we let the swarm converge to their optimal position (equivalently, to the optimal hyperparameter combination), and then we solve the imaging RML problem with the optimal weights.

In contrast with MOEA/D, MO-PSO formulation allows to obtain the marginal contribution of every regularizer. In other words, instead of exploring the whole effects of each regularizer over the data terms, it seeks the best compromise among all the functionals.

By letting the population evolve enough, individuals converge to a set of non-dominate solutions (see Pardalos et al. 2017; Müller et al. 2023, for definition) that approximates the Pareto front. Therefore, a explicit dependency (manifold) between dataterms and regularizers can be obtained.

4. Scattering screen reconstruction

In this section, we validate the algorithm's performance at high frequencies, in particular, at 230 GHz. In this regime, scattering corruptions are minimal, thereby providing a clear framework for assessing the efficacy of the mitigation strategy. In subsequent sections 5 and Appendix 5, we investigate the algorithm's behavior at lower frequencies, where the corruptions are stronger and the problem is more constrained.

4.1. Stochastic Optics scattering screen discretization

First, we present (Johnson 2016) theoretical framework on Stochastic Optics, followed by the strategy we have used to mitigate the scattering.

The Johnson (2016) framework represents $\phi(r)$ in the Fourier domain, with uncorrelated complex Gaussian variable components

$$\tilde{\phi}(\mathbf{q}) = \int \phi(\mathbf{r}) e^{-i2\pi\mathbf{q}\cdot\mathbf{r}} d\mathbf{r}.$$

The time-averaged power spectrum is given by

$$\langle |\tilde{\phi}(\mathbf{q})|^2 \rangle = A_\phi Q(\mathbf{q}),$$

where A_ϕ is the screen area over which the Fourier transform is computed (see, e.g. Blandford & Narayan 1985).

The power spectrum associated with the observed visibilities is given by

$$Q(\mathbf{q}) = 2^\alpha \pi^\alpha \frac{\Gamma(1 + \alpha/2)}{\Gamma(1 - \alpha/2)} \lambda^{-2} (r_{0,x} r_{0,y})^{-\alpha/2} \times \left[\left(\frac{r_{0,x}}{r_{0,y}} \right) q_x^2 + \left(\frac{r_{0,y}}{r_{0,x}} \right) q_y^2 \right]^{-(1+\alpha/2)}, \quad (13)$$

where x, y are the coordinates aligned with the major and minor axes of the diffractive kernel. We consider the screen to be located at $M = 0.43$ as stated in Bower et al. (2014).

The scattering phase screen (in radians) is parameterized using an $N \times N$ grid of Fourier coefficients $\tilde{\phi}_{o,s}$:

$$\phi_{l,m} = \frac{1}{\sqrt{A_\phi}} \sum_{o,s=0}^{N-1} \sqrt{Q(o,s)} \epsilon_{o,s} e^{i2\pi(l o + m s)/N}.$$

being $\epsilon_{o,s} = \frac{\tilde{\phi}_{o,s}}{\sqrt{Q(o,s)}}$. In this way, Johnson (2016) parameterize the unknown phase screen as a set of $\frac{N^2-1}{2}$ variables.

Once $\epsilon_{o,s}$ has been specified for a particular field of view, the corresponding scattering can be computed for any desired observing wavelength. We adopt this framework to model Eq. (11).

Therefore, the mitigation can be summarized as follows: given observation data, we try to find the best image that fits it and whose power spectrum is close to Eq. (13). For every reconstruction, we compute its power spectrum and we minimize along the χ^2 axis. We denote this functional as R_{SO} . Mathematically,

$$R_{SO} := \sum |\epsilon_{o,s}|^2.$$

Johnson et al. (2017) solves the optimization problem

Problem 3 (Johnson et al. (2017) Stochastic Optics version).

$$\min_{x \in D} R_{entr} - \alpha_1 f_8 - \alpha_2 R_{SO}, \quad (\text{JohnsonSO})$$

being R_{entr}, f_9 the functionals described in Eq. (10) and Eq. (12) respectively fixing only one frame ($j = 1$) and without wavelets coefficients applied.² There are some limitations

- The lack of multimodal exploration in the context of highly non-linear non-convex functionals and the use of gradient-based approach limits the exploration on screen modeling. To overcome this limitation, standard approach performs a survey on the different hyperparameters of the optimization problem.
- The inclusion of an additional hyperparameter increases the dimensionality of the problem, potentially reducing the efficiency of the survey strategy. This is translated in much slower algorithm. In addition, the SO algorithm is slower than regular imaging due to the discretization of the screen and the computation of the power spectrum, which complicates and increases the cost of

² Indeed, Johnson (2016) only consider the visibilities as data terms, however **eht-imaging** library (Chael et al. 2016, 2018) has the extended version.

the imaging problem. As a result, the associated optimization process converges more slowly or requires more time to complete the same number of iterations as in a standard imaging problem. This challenge is particularly pronounced for large datasets.

- Effects of the screen are not simple. To understand those effects, a full marginalization would be better.

In contrast, the flexibility of multiobjective optimization enables the immediate integration of R_{SO} within complex frameworks, allowing the method to leverage several advantages. These include avoiding costly hyperparameter explorations and achieving a balanced optimization with other regularizers beyond R_{entr} . For example, MOEA/D facilitates exploration of the Pareto front and identification of different local minima, which is particularly crucial for very sparse observations weakly affected by refractive noise, such as those from the EHT or ngEHT (Raymond et al. 2021; Chavez et al. 2024) at 230 GHz. Similarly, MO-PSO offers a straightforward way to determine the marginal contribution of the regularizer, such as the screen’s impact on the data. In this way, the three limitations of the method proposed by Johnson (2016) are addressed.

4.2. Synthetic Data generated at 230 GHz

To assess the performance of our modeling, we have tested it across various synthetic structures created with `eht-imaging` library (Chael et al. 2018), supposing static and dynamic screens at 230 GHz. The simulated datasets include different levels of realistic gain corruptions. In the following sections, we show the results.

There are no updates to the modeling of the screen itself in this manuscript, but rather to the way the optimization problem associated to its reconstruction is solved. The major improvement that we are claiming stems from the correct modelling of the multimodality of the problem, i.e. of the degeneracies associated with the fact that different realizations of the scattering screen and the on-sky emission could produce similar visibilities. We identified three scenarios for which this strength could be exceptionally beneficial. First, at 230 GHz observations, even with a static source and a static screen, the effect of the scattering is small, expected to be degenerate with the noise realization. Moreover, if the scattering has a speed associated to it, the dynamics of the screen could be misidentified with small-scale corruptions in the actual image. And finally at 86 GHz, the screen obscures the image and significantly worsens the instrumental resolution, leading to a situation for which small-scale structures at the $20 \mu\text{as}$ scales typical for the EHT could be attributed to the effect of the scattering screen or the internal features of the emission. The test cases discussed in this manuscript address these three scenarios.

As a first and simplest example, we have simulated a static ring with an asymmetric brightness distribution observed during the best time window (Fig. 1 top left panel). This time window spans approximately 100 minutes and presents the best uv-coverage, isotropy, and (u, v) coverage fraction for Sgr A* in April 7, 2017 during the EHT campaign (more details can be found in Farah et al. 2022; Event Horizon Telescope Collaboration et al. 2022c)³. Fig. 1 top left panel depicts the corresponding the uv-coverage.

³ The election of this window will be justified in latter sections.

Gain corruptions of 4% and 10% have been included in the data. Additionally, we have corrupted the observations with several synthetic screens simulated using the `StochasticOptics` (Johnson 2016) module of `eht-imaging` library. Fig. 1 bottom panel shows the effects of the refractive noise on the longer baselines for the two levels of gain corruptions. We demonstrate how we are able to recover both the intrinsic descattered source and the scattering screen, as well as and how the screen prior is important in this poorly constrained problem.

In a second step, we increase the difficulty by simulating a population of different geometric sources affected by scattering screens with different velocities. We demonstrate its capability to recover the (dynamic) scattering screen even assuming 10% gain corruptions. We would like to note that this scenario is only a first step towards constructing an algorithm able to adapt to real data. In EHT data, Sgr A* shows significant variability stemming from the evolution of the source itself rather than the dynamics of the scattering screen (e.g. Event Horizon Telescope Collaboration et al. 2022a; Wielgus et al. 2022). Any algorithm would need to separate the effect of the source dynamics from the effect of the scattering and the screens internal variability. Correctly modeling the dynamics of Sgr A* is a challenging, but independent, problem on its own (even without scattering) with a wide range of proposed solutions (Bouman et al. 2017; Event Horizon Telescope Collaboration et al. 2022c; Müller & Lobanov 2023a; Roelofs et al. 2023; Mus & Martí-Vidal 2024; Mus et al. 2024b,a). Here, we rather study the simpler question: For a static source scattered by a screen which is dynamically evolving, can we recover the speed of the screen correctly? Despite its simplicity, it yields two important outcomes. First, successfully demonstrating this capability helps constrain the currently broad range of expected screen velocities ($\sim 50 \text{ km/s}$ to $\sim 200 \text{ km/s}$ Gwinn et al. 1991; Reid et al. 2019). Second, it needs to be demonstrated before establishing a framework that solves us the more complex scenario in which both the source and the screen are dynamic.

4.3. Recovering the screen: Algorithm

The strategy we have used is summarized in Algorithm 1. First, we define a prior image and a prior screen. Throughout this paper, we understand the concept of prior as the initial point of a minimization algorithm. For the case of 230 GHz data, we use as a $60 \mu\text{as}$ symmetric Gaussian as a prior. Then, we compute the wavelet coefficients, Ψw_I , as described in (Müller & Lobanov 2022) to help overcome the sparsity of the data. These inputs are used to define a composite vector x that encapsulates the image and scattering information, with an overall dimension of $2n_{\text{pix}}^2 - 1$. In the first optimization step, the algorithm applies MO-PSO, using the prior image as the starting point. This optimization is carried out over P_0 particles and K_0 iterations, yielding an intermediate solution x_{img} that is selected based on optimal regularization criteria.

The next stage involves redefining the prior as a combination of the optimized image x_{img} and the initial prior scattering screen. This updated prior serves as the initialization for a second MO-PSO run, which aims to further refine the solution by optimizing both the image and scattering screen simultaneously. This stage uses P_1 particles

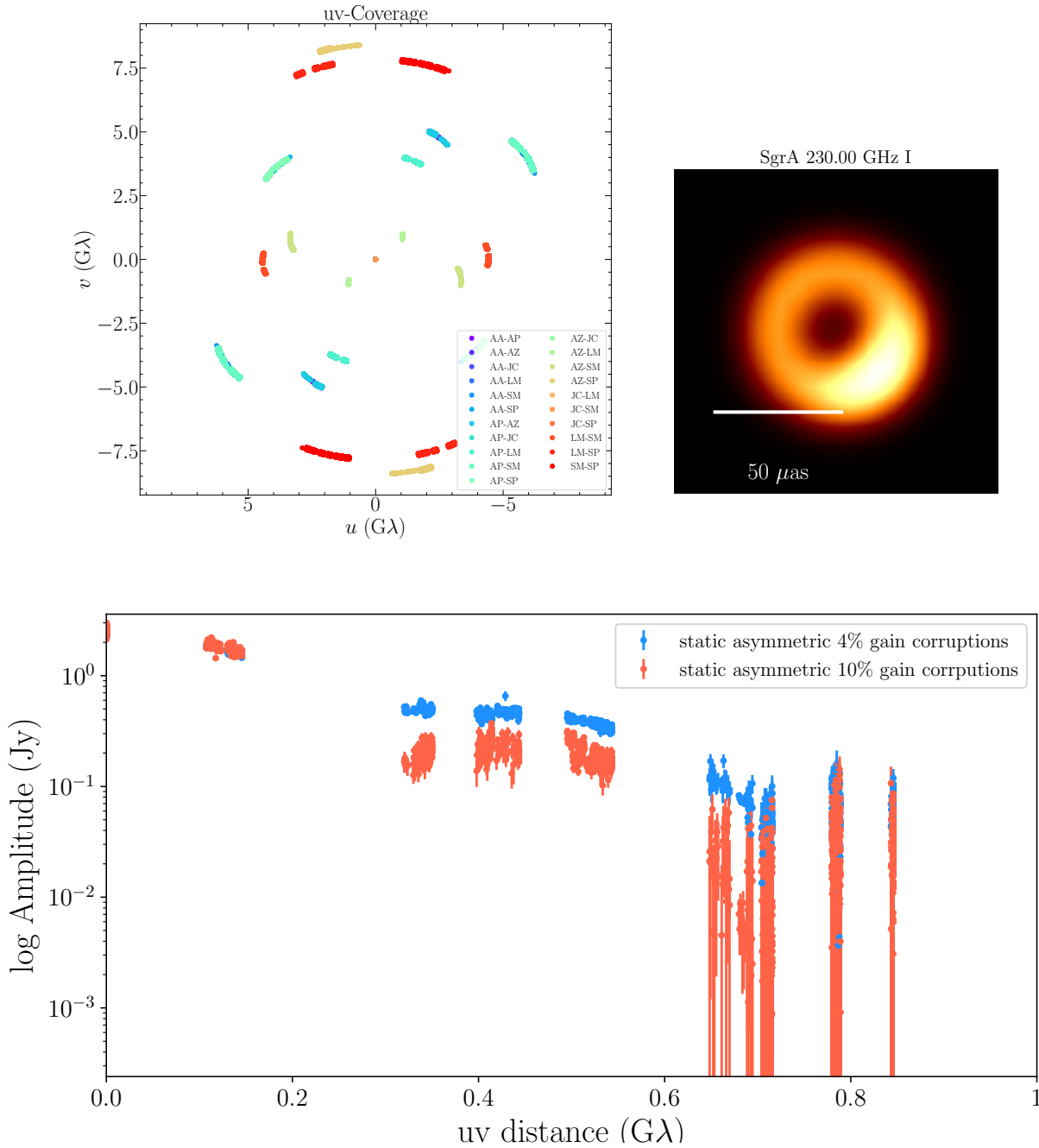


Fig. 1: Top left panel: uv-coverage for Sgr A* in the best time window of April 7, 2017. Different colors represent different baselines (indicated in the legend). Top right panel: simulated ring in that coverage, with a brightness asymmetry. Bottom panel: log amplitude vs uv distance for the static scattered asymmetric ring with different gain corruptions: Blue, 4% and red 10%.

and K_1 iterations, ultimately producing a final image with minimized scattering effects.

4.4. Results

Throughout this paper we evaluate the results by using the normal-cross-correlation⁴, or **nxcorr** metric (see Event Horizon Telescope Collaboration et al. 2019d; Farah et al.

⁴ A measure to compare two images. The closer the value is to 1, the more similar the two images are

2022, for formal definition). In Table C.1 of the Appendix C, all the **nxcorr** values for all images can be found.

4.4.1. Different gain corruptions

In these paragraphs, we suppose a screen of 50 km/s in East direction during the whole observation.

Figure 2 presents the result of the Algorithm 1. Top row is the case of 4% gain corruption, and bottom row 10%. From left to right, it begins with the scattered asymmetric ring presented in Fig. 1. Then, the true scattering screen. Third and fourth panels show the recovered (descattered)

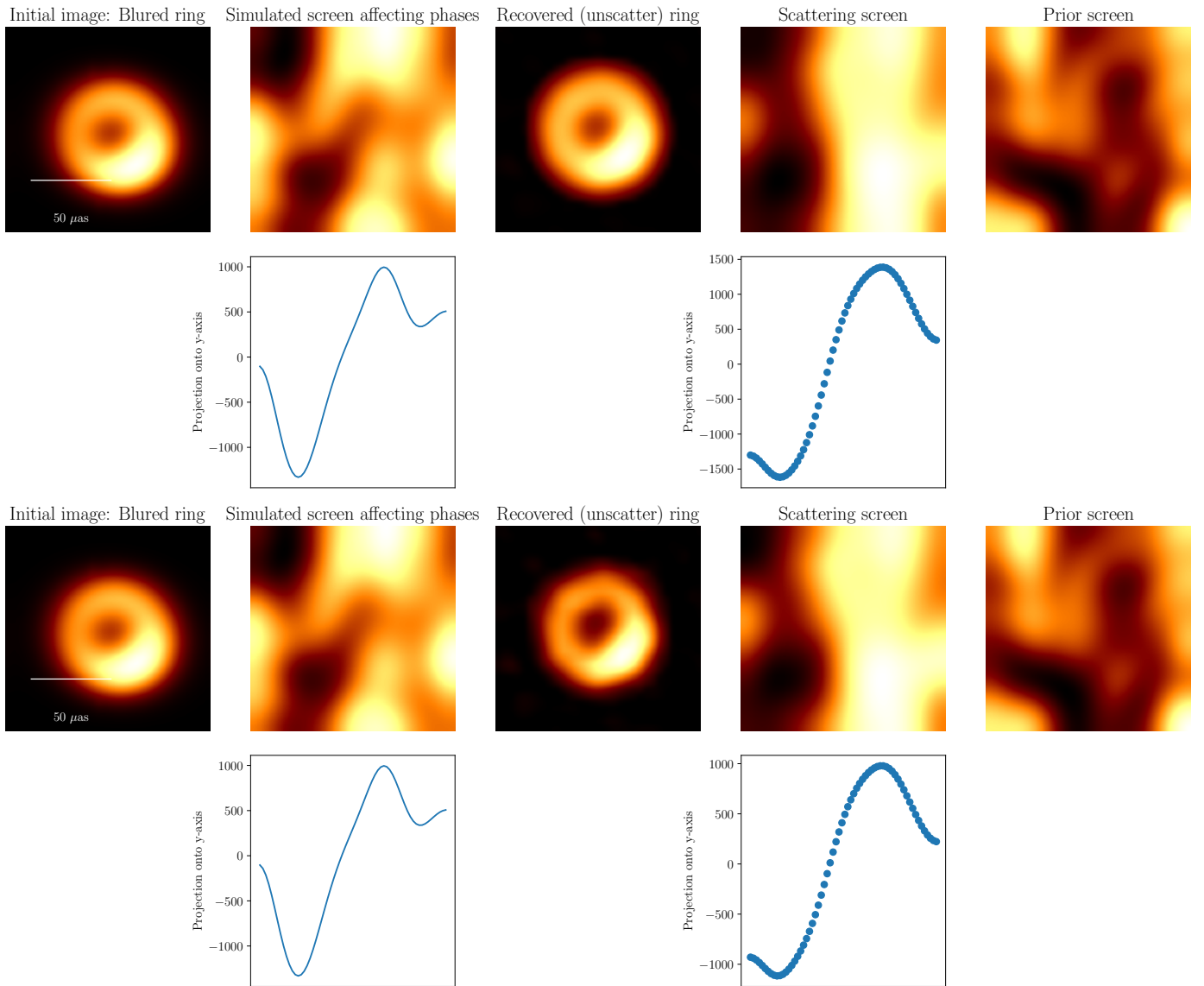


Fig. 2: Scattering reconstruction using MO-PSO of the static ring with asymmetric brightness distribution with thermal noise and 4% gain corruptions (top row) and with thermal noise and 10% gain corruptions (bottom row). From left to right: simulated blurred ring, ground-truth screen, recovered intrinsic structure, recovered screen and prior screen. The screens have been convolved with the instrumental beam. Subplots below the second and fourth panels depict the projection on the y-axis of the brightness distribution along the right ascension.

ring and the predicted screen resulting from Algorithm 1. Finally, the prior screen is depicted in the last panel. Because the screen at this high frequency is poorly constrained and the uv-coverage is very sparse, a uniform screen (in contrast with the proposal of Johnson 2016) is not a valid starting point.

In both cases, the recovered scattering screen are compatible, and they show some similarities to the real one in the sense that roughly the positions of the brightest spots are recovered and depressions are also kept, as visible when we inspect the projection along the y-axis of the recovered screen with the true screen (second and fourth row). However, we would like to note that none of the finer structure in the simulated screen got recovered correctly, and the localization of the peaks and troughs is also not very accurate. This is probably expected, given the challenges of an array such as the EHT and the small effect of the screen at 230

GHz. Moreover, since the effect of the screen is very small at 230 GHz, the resulting, descattered image is similar to the on-sky image, i.e. the on-sky image already shows a ring structure.

4.4.2. Prior screen independence

As discussed above, a physically feasible screen prior is needed to recover the screen in this case with high degrees of freedom and very sparse uv-coverage. To ensure the algorithm is not prior biased, we present two tests, where the asymmetric ring has been scattered with the same true screen, but two different initial screens have assumed.

Figure 3 shows the two cases assuming 10% systematic errors. We can appreciate how the reconstructed screen is indeed different. However, the main features, as the brightest areas and the depressions, are recovered. In particular,

Algorithm 1 Scattering mitigation using PSO

Require: observation uv data.

Require: prior image (dimensions npix^2), wavelet coefficients, prior screen (dimensions $\text{npix}^2 - 1$).

Define an image as a vector, x of dimension $2\text{npix}^2 - 1$.

Run MO-PSO using $x_0 \leftarrow$ prior image, P_0 particles and K_0 iterations to solve the imaging problem. Solution x_{img} is the one with optimal regularizer values.

Define prior = $[x_{\text{img}}, \text{prior screen}]$.

Run MO-PSO using $x_0 \leftarrow$ prior, P_1 particles and K_1 iterations to solve the imaging problem.

we can deduce that the prior screen (even if it is not similar to the real one) can help the algorithm to converge to a better screen. Nevertheless, since the refractive noise is not the dominating noise, and it is low constrained, differences on the intrinsic structure reconstructions are negligible. This difference is also represented in the slightly different values of the `nxcorr` shown in Table C.1.

4.4.3. Different screen velocities

Next, we attempt a more challenging test case. We try to recover the speed of the scattering screen (on a static source). As discussed above, this is an artificial experiment since in practice also Sgr A* is evolving dynamically. However, we defer the full analysis of the source dynamics together with a moving screen to a consecutive work. In the dynamic regime, it is essential to investigate whether the temporal evolution of the scattering screen impacts each frame of the observation. For that, we have simulated a screen at different velocities affecting static geometric sources based on the best time window coverage and corrupted by thermal noise. In particular, we have simulated two screens at two different velocities, one at 50 km/s based on observations of Gwinn et al. (1991) and one at 200 km/s, Reid et al. (2019). For a scattering screen velocity of 50 km/s, the effects of the kinematics of the screen over 100 min period are minor, whereas velocity of 200 km/s produces noticeable effects. Therefore, in any dynamic study, the speed of the screen needs to be properly constrained.

To study the effects of the speed, we solve MO-PSO + SO for every keyframe.

The weak refractive noise effect on the data implies that the speed velocity does not affect the intrinsic structure recovery. Fig. 4 depicts a comparison of the same scattered source (first panel), a crescent, affected with same screen moving at different velocities (upper row 50 km/s, lower row 200 km/s).

To illustrate the screen's evolution, we have projected the pixel brightness distribution along the y-axis and plotted it as a function of time, following a similar approach to that described by Mus & Martí-Vidal (2024). This will be called cylindrical plot. The third and fourth panels display the recovered intrinsic source structure and the corresponding recovered evolution of the scattering screen, respectively. Note that the simulated screen was moving along the x-axis, so the projection is done orthogonal to the di-

rection of motion. The cylindrical plots (second and fourth column) can be understood as the logical extension to the projections shown in Fig. 2, i.e. every column of the plotted matrix corresponds to the projection along the y-axis of the true/recovered scattering screen at the respective frame in time.

We recall from our discussion above, that while the reconstruction of any structural feature finer than roughly $20 \mu\text{as}$ is not recovered, even in the static case. However, the broad, overall structure of approximate positioning of troughs and peaks across the field of view can be identified. Fig. 4 now demonstrates that we can even track this evolution in time, and hence effectively measure the speed of the screen from the reconstruction by the gradient in the cylindrical plots.

4.4.4. Different intrinsic structures

Figure 5 presents the results of the same experiment with different observed sources. It illustrates how the geometry of the sources can significantly impact the difficulty of recovering the (dynamic) screen. In the case of the disk (bottom row), the recovered screen's cylindrical plot is noticeably less noisy compared to that of the ring (top row). The null in the uv-plane is influenced by the screen, making the imaging problem more challenging to be solved. Nevertheless, we succeed in measuring the speed of the screen correctly with an error smaller than 10 km/s.

5. Prospects of imaging Sgr A* ring at 86 GHz

While at 230 GHz our method successfully recovered the screen's overall dynamics and morphology, it could not capture small-scale structures (as predicted and shown in Johnson 2016) because the refractive noise was poorly constrained. In contrast, at 86 GHz this noise is expected to be more constrained on longer baselines, potentially allowing finer structural details to be recovered.

In this section, we explore the prospects of recovering ring structures in the GMVA frequency regime. To achieve this, we have exploited the multimodality capabilities of MOEA/D. We have simulated observations using the 2025 GMVA configuration, incorporating ALMA (Atacama Large Millimeter/submillimeter Array) stations, including NOEMA and a double bandwidth.

Static 86 GHz. Including gain errors

Using `nghtsim` (Pesce 2022), we have simulated static ring observations with a shadow diameter of $\sim 50 \mu\text{as}$, emulating that reported by the EHT (Event Horizon Telescope Collaboration et al. 2022a). We assumed bad weather conditions to decrease the SNR, and we included thermal errors, as well as 4% gain errors in phases and amplitudes. The aim is to verify if the intrinsic ring structure can be recovered. Figure 6 shows the uv-coverage corresponding to the simulated array (left panel) and the SNR versus uv-distance (right panel).

In the range of 86 GHz, scattering effects dominate over the noise and so the image is strongly affected, having a Strehl ratio of $S \sim 0.6$ (see Fig 1 from Johnson 2016). That is to say, refractive noise at longer baselines is much more constrained, leaving less degrees of freedom to recon-

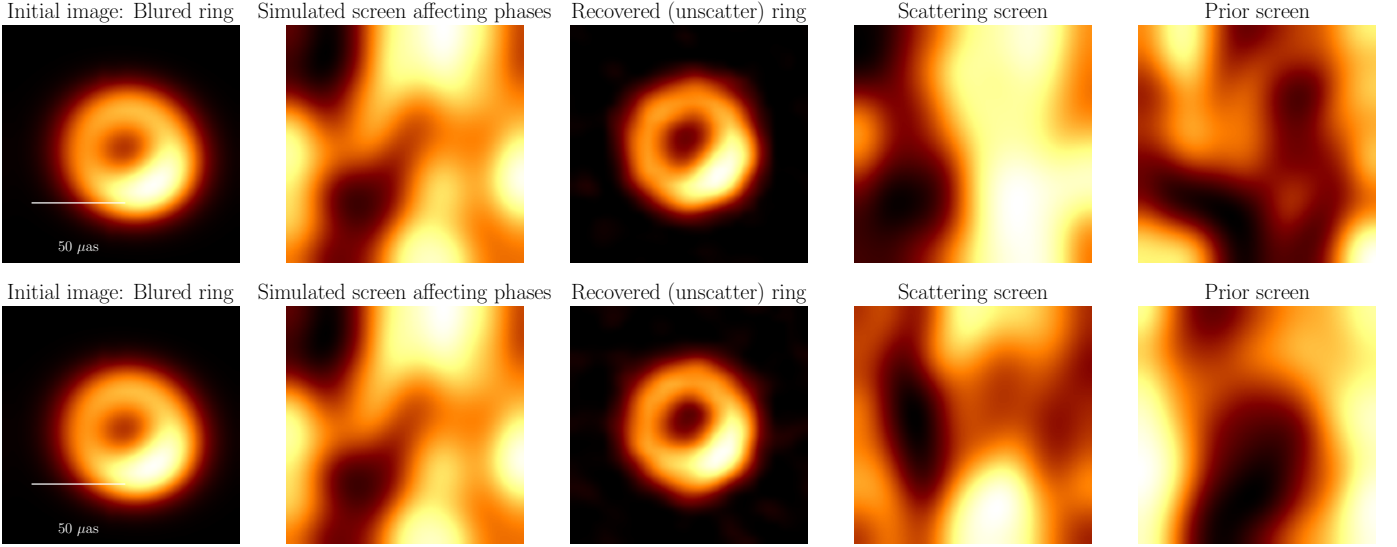


Fig. 3: Comparison of the scattering reconstructions of the ring with asymmetric brightness with different screen priors. The screens have been convolved with the instrumental beam.

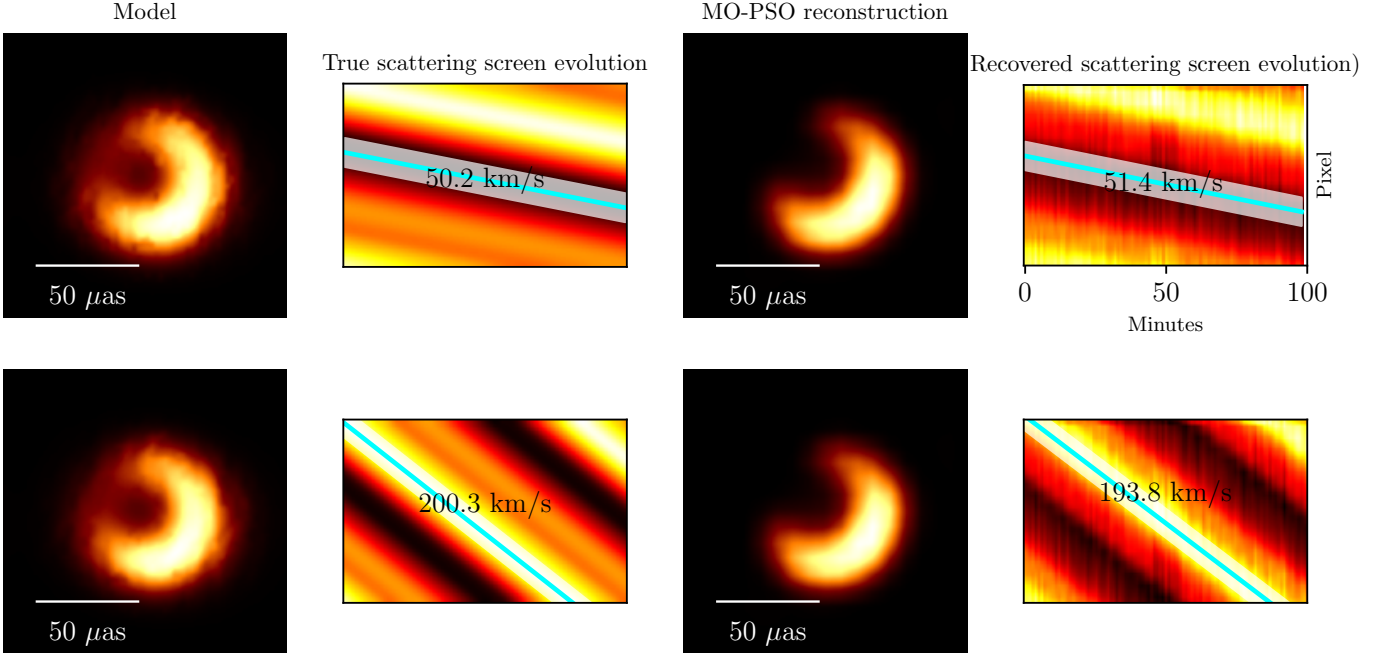


Fig. 4: Demonstration of scattering screen velocity recovery of a screen affecting a static crescent. Top row: The true scattering screen evolves at 50 km/s (center-left panel), while the recovered velocity is 51.4 km/s (right panel). Bottom row: The true scattering screen evolves at 200 km/s (center-left panel), while the recovered velocity is 193.8 km/s (right panel). The slight deviation from the exact velocity are due to numerical errors in the fitting procedure. The left and center-right panels show the corresponding reconstructed crescent for each case.

struct the screen. In any case, a careful mitigation strategy is crucial.

Due to the complex structure of the screen and the steep brightness gradients that can occur between nearby pixels, genetic algorithms may struggle to converge rapidly to an optimal solution. To address this issue, we have run MO-PSO starting with the cluster containing the higher number of local minima or the most probable solution, which is also the most probable solution based on the RML method (although any other cluster could also be chosen; see Müller

et al. 2023; Mus & Martí-Vidal 2024, for further details), as the initial starting point. By starting in a neighbor of a local minimum we can exploit gradient-based algorithms to quickly find a solution. Moreover, MO-PSO ensures convergence to the solution with optimal regularizer contributions.

The strategy we have used is described below and summarized in Algorithm 2. We initialize the MOEA/D algorithm with a population of 340 individuals and 51 neighbors. For the entropy prior, we assume a uniform Gaussian of 60, μas . The first generation of individuals is initialized

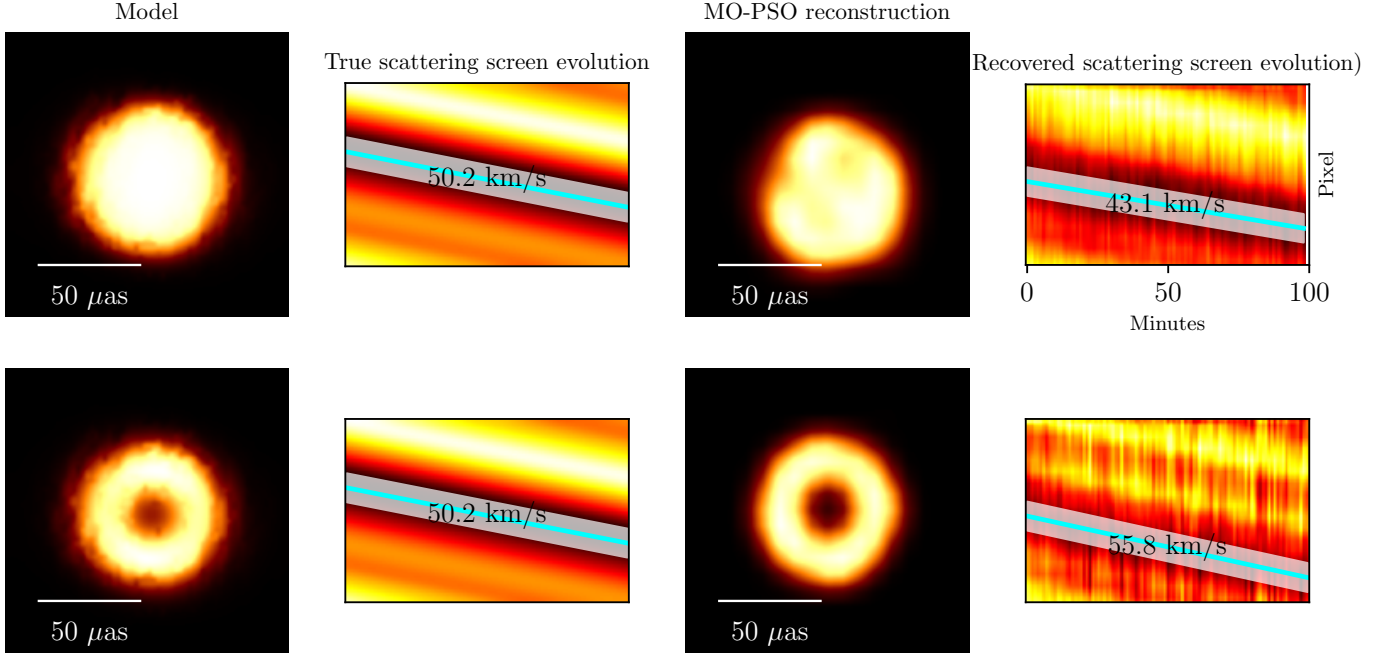


Fig. 5: Dynamic scattering reconstruction equivalent to the one in Fig. 4 but with different intrinsic sources. Ring top and disk bottom.

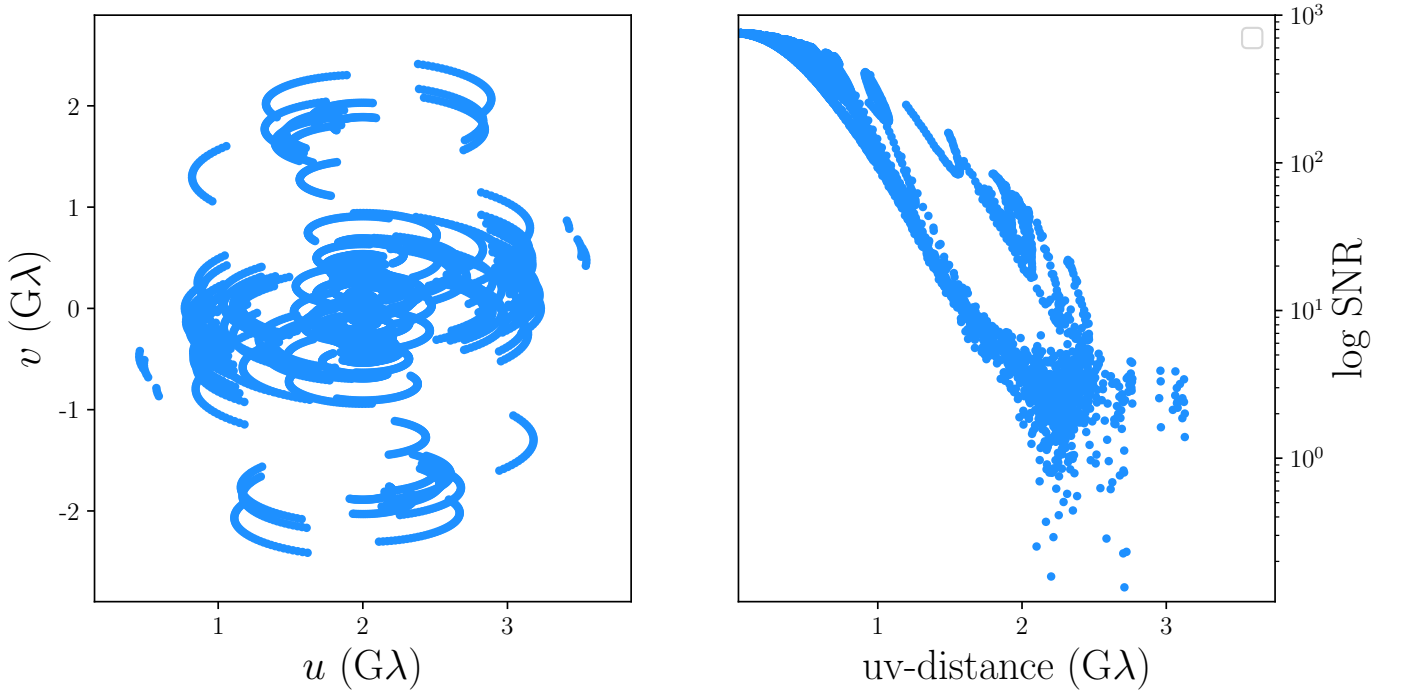


Fig. 6: uv-coverage for the GMVA + ALMA array observing Sgr A* at 86 GHz (left panel) and signal-to-noise ratio in log scale vs uv-distance (right panel). The bad weather conditions and the 4% gain corruptions, provoke a low SNR even in the case of ALMA baselines.

with a Gaussian whose beam parameters are taken from the least-squares (LSQ) Gaussian fit reported by Issaoun et al. (2019), with values of $(120, \mu\text{as}, 100, \mu\text{as})$ and a position angle (PA) of 90 degrees. Data with a SNR below 10, equivalent to approximately 1.25% of the maximum SNR, are flagged. We consider the data terms of MOEA/D to be

closure quantities (phases and log-amplitudes). We let the population evolve over 1000 generations. After the population has finished evolving, we cluster the 340 individuals (solutions) by similarity, requiring 10% similar features to belong to the same cluster. We pick a representative image from the cluster that contains more solutions (the most

Algorithm 2 Scattering mitigation - Exploring multi-modality

Require: observation uv data.

Require: prior image (dimensions npix^2), prior screen (dimensions $\text{npix}^2 - 1$).

Require: $n \leftarrow$ local minima to be explored, $N \leftarrow$ number of selfcalibration iterations.

Define an image as a vector, x of dimension $2\text{npix}^2 - 1$.
 Create a population of n images and a 8-dimensional mesh of k vertices to grid the space.
 Define x_0 to be the Gaussian seen in Issaoun et al. (2019).

[Optional] flag low SNR sites

for $i = 1, \dots, N$ do

 Run MOEA/D to get n local minima.

 Clustering solutions by similarity: Pick the most cluster containing more solutions, and call it x_i .

 Selfcalibrate the visibilities with x_i .

 Recenter the image, if needed.

$x_0 \leftarrow x_i$.

end for

$x_{\text{MOEA/D}}^* \leftarrow x_N$.

Run MO-PSO using $x_0 \leftarrow x_{\text{MOEA/D}}^*$, P particles and K iterations.

probable local minimum), we selfcalibrate N times, running in every iteration MOEA/D, using this image as a starting point and let the new population (composed, again, of 340 individuals and 51 neighbors) evolve over 500 generations.⁵ If needed, we recenter the source to the (0,0) since the relative position information can be lost due to the use of closures. Fig. B.1 shows the set of clusters for 3 iterations. The clusters surrounded by a green box are the one with higher **nxcorr** compared to the simulated model. The red box marks the cluster containing more solutions, and the blue box the cluster with better hyperparameter combination. The solution obtained after the last selfcalibration iteration is used as starting point to solve MO-PSO. The faster convergence of MO-PSO allows to obtain a more accurate solution faster. Fig. 7 shows the final source and screen reconstruction. The intrinsic structure has a **nxcorr** of 0.97, while the recovered screen of 0.81 (blurred) and 0.88 (non-blurred). These metrics demonstrate how successful the algorithm was recovering a screen in a more constrained case.

In next section we apply MOEA/D with different starting points and report the probabilities of obtaining a ring solution under optimal conditions using a priori calibrated data. Our findings indicate that, for certain initial conditions, convergence to a ring solution is unattainable, whereas for others, such as a Gaussian starting point, the probability remains low but a ring can indeed be recovered.

Static 86 GHz. A priori calibrated data with thermal noise only

In this section, we explore the chances of obtaining a ring structure using different starting points when having a pri-

ori calibrated data only corrupted with thermal noise. The goal of this section is to demonstrate the importance of the global exploration and how the assumed starting geometry may condition the problem, making impossible to recover a ring even in favorable situations. The strategy used is summarized in Algorithm 3. The three starting points are: Gaussian observed by Issaoun et al. (2019) using LSQ before applying SO (major FWHM of $228 \mu\text{as}$, minor FWHM of $143 \mu\text{as}$ and PA of 86 grad), a disk of $60 \mu\text{as}$ and a ring with the expected shadow size seen by the EHT of $50 \mu\text{as}$ (Event Horizon Telescope Collaboration et al. 2022a). Fig. A.1 shows the images (top row) and their amplitude vs uv-distance in log scale (bottom row).

For every case, we have explored ~ 360 local minima and we let the population to evolve during 10000 generations, with allowing each individual to interact (cross-over) with the 15% of the population. The dataterm functional now is the χ^2 of the visibilities.

Figure B.2 presents the Pareto fronts of the solutions originating from three distinct starting points—Gaussian, disk, and ring—each clustered using a uniform “similarity threshold” of 10%. The title of each cluster indicates the percentage of solutions contained within it, along with the χ^2 value quantifying the discrepancy between the true unscattered ring and the reconstructed image.

First thing to notice is the different number of clusters every starting point contains. The starting point conditions the diversity of the recovered solutions. Then, we can notice how we can recover the ring starting from a Gaussian but not from a disk, meaning that the optimization algorithm tends to find faster disk structures than ring. Therefore, optimization needs to start from a distant point. Another interesting fact is χ^2 is systematically lower in all the clusters presenting ring-like structures. Therefore, even if the rest of the clusters may approximate the Pareto front (i.e., are local minima, valid images), the ones with the ring are the ones presenting the best fit to the data.

Table 1 summarizes the results of the MOEA/D exploration with the different starting points. For the Gaussian starting point, we find that 25.45% of the solutions are ring-like (~ 85 local minima). That means that the probability of finding a local solution that represents a ring is just ~ 0.25 . Therefore, unimodal optimization methods (based on gradients or Hessian) are likely to find a non-ring solutions. In contrast, using a ring with the expected size of Sgr A* as initial point increases the probability to almost to 40%. Although considering a ring as initial point maybe a strong bias, we can claim that with two completely different starting points, MOEA/D is able to recover ring.

Thus, we conclude that the choice of prior complicates the accurate recovery of the true source structure. In this context, standard local searches struggle to explore alternative candidates, making them suboptimal strategies for identifying lower-probability solutions in a highly ill-posed problem.

Conclusions

We have investigated the feasibility of recovering Sgr A*’s ring structure at 86 GHz in the presence of refractive scattering and various observational challenges. The refractive noise at this lower frequency, although dominant, is more strongly constrained on longer baselines than at 230 GHz, allowing our global optimization schemes (MOEA/D fol-

⁵ We run 500 generations to speed-up the process.

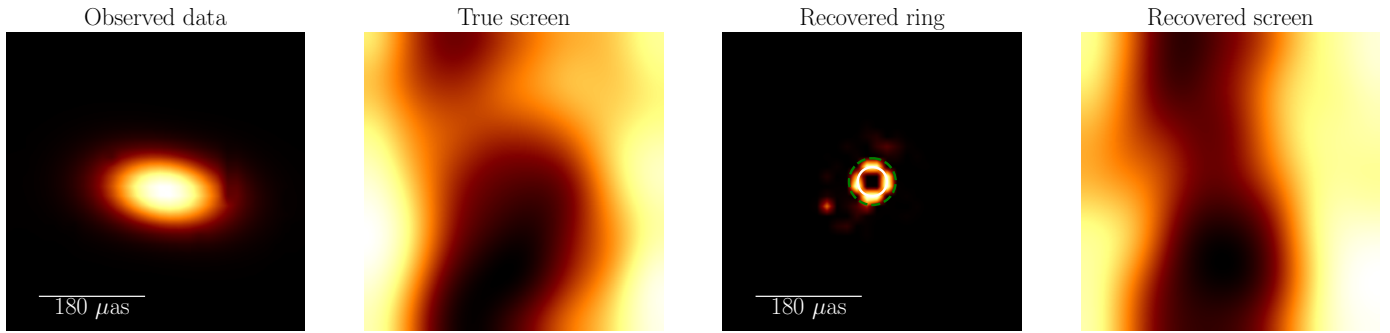


Fig. 7: Scattered ring observed at 86 GHz (first panel) with 4% gain corruptions. Second panel shows the simulated screen affecting the source. Third panel depicts the recovered solution using Algorithm 2. White internal circle shows the shadow’s diameter of the simulated ring ($50 \mu\text{as}$), green dashed circle is 1.6 times the size of the shadow, as predicted by Lu et al. (2023); Kim et al. (2024b) in M87*. Fourth panel is the recovered screen. Screens are blurred to the GMVA resolution. `nxcorr` can be found in Table C.1.

	Number of clusters	Number of ring clusters	Total ring solutions (%)
Gaussian	9	2	25.45
Disk	4	0	0
Ring	5	2	37.57

Table 1: Overview of clustering results for initial points used in the MOEA/D algorithm. The table shows the total number of clusters identified with a 10% similarity threshold, the number of those clusters that present a ring structure, and the percentage of total solutions (out of 340) that exhibit ring-like morphologies.

Algorithm 3 Scattering mitigation - Exploring multi-modality without selfcal

Require: observation uv data.

Require: prior image (dimensions npix^2), prior screen (dimensions $\text{npix}^2 - 1$).

Define an image as a vector, x of dimension $2\text{npix}^2 - 1$.
Create a population of n images and a 8-dimensional mesh of k vertices to grid the space.

Run MOEA/D to get n local minima.

Clustering solutions by similarity: Pick the cluster with less χ^2 , $x_{\text{MOEA/D}}^*$.

Run MO-PSO using $x_0 \leftarrow x_{\text{MOEA/D}}^*$, P particles and K iterations.

lowed by MO-PSO) to resolve finer structural features. Even under adverse conditions—such as low signal-to-noise and gain errors—the proposed multi-step strategy robustly recovers both the intrinsic source geometry and a meaningful approximation of the scattering screen, with final `nxcorr` values as high as 0.97 for the source.

Moreover, we have demonstrated that the choice of initial image geometry significantly influences whether the optimization converges to a ring solution. In idealized simulations with a priori calibrated data, starting from a Gaussian prior yields roughly a 25% chance of recovering a ring, whereas beginning with a ring prior raises that probability to nearly 40%. By contrast, a disk prior never converges to a ring solution in our tests. These findings underscore the importance of genuinely global exploration methods and the

use of diverse initial conditions when imaging strongly scattered sources like Sgr A*. Overall, a comprehensive, multi-modal approach is essential to mitigate the ill-posed nature of VLBI data at 86 GHz and reliably recover ring-like structures in the presence of refractive scattering.

6. Marginal contribution of SO regularizer

To conclude the analysis, we examine the marginal contribution of the Regularizer (11) at frequencies of 230 GHz and 86 GHz. We have followed a strategy similar to that outlined in Mus et al. (2024a): running MO-PSO with the same initial point, number of iterations, simulated screen, and number of particles, but varying the initialization of these particles by following a uniform distribution. This approach allows us to assess the impact of the regularizer across different refractive noise conditions. Using MO-PSO, we can determine the relative importance of a given regularizer on the final reconstruction. This information constrains the possible values of the regularizer. The lower the variance in the values, the more constrained and significant the regularizer is for the reconstruction.

Figure 8 shows the distribution of the values of the hyperparameter for both frequencies. As expected, we note a broader distribution for 230 GHz, meaning that the regularizer is less constrained. Table 2 summarizes the main features. The standard deviation (std) for 230 GHz is, indeed, larger than for 86 GHz

7. Future work

This work opens several promising directions for future investigation.

First, the `nxcorr` metric has been found to be suboptimal for validating our results, as elaborated in Appendix C.

Table 2: Mean, standard deviation, minimum and maximum values of the hyperparameter associated to Eq. (11).

	mean	std	min	max
Frequency (GHz)				
86	521.175708	248.024702	1.600457	960.440496
230	490.462748	282.973316	3.254598	989.571094

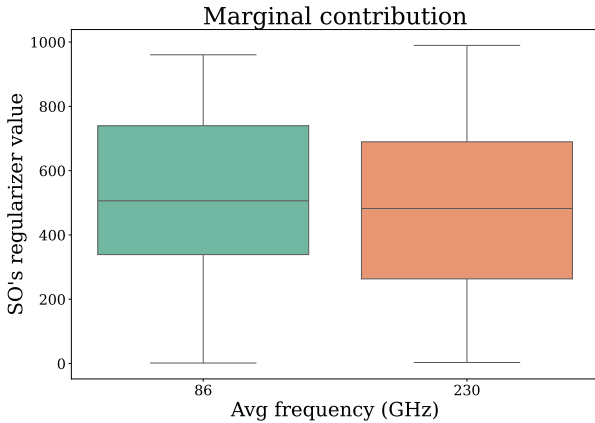


Fig. 8: Marginal contribution of the hyperparameter associated to Eq. (11) for observations at 86 and 230 GHz.

While the main features of the reconstructions may be recovered, the metric values often do not accurately reflect the visual quality of the outcomes. In future works, we will aim to find a better and appropriate metric that successfully reflects the fidelity of the reconstructions.

Second, in the current study Sgr A* has been considered a static source. However, the reconstruction of the scattering screen in Sgr A* may present an additional challenge due to the intrinsic variability on minute timescales of this source (Event Horizon Telescope Collaboration et al. 2022c). A wide range of movie-making algorithms that account for time-domain correlations have been proposed in the past (Bouman et al. 2017; Müller & Lobanov 2022; Roelofs et al. 2023; Mus & Martí-Vidal 2024; Mus et al. 2024b,a). The recent studies on the dynamics of Sgr A* at horizon scales Event Horizon Telescope (2025), future research will focus on incorporating Sgr A* as a dynamic source and also a dynamic scattering screen to achieve reconstructions of real data by better capturing the system's time-dependent behavior.

Third, we are investigating how the intrinsic geometry of the initial conditions influences the multimodality exploration. We have observed that starting the exploration with certain geometric models, for example, disk, makes impossible to recover the intrinsic ring, while using a Gaussian as an initial point allows us to recover ring structures in the $\sim 25\%$ of occasions (see Appendix 5 for further details). Another case we aim to understand is why the reconstruction of the scattering screen appears noisier when applied to a ring structure, as indicated in Fig. 4.

Fourth, we intend to apply this strategy to real data at 86 GHz, observed with the new sites and capabilities of the GMVA+ALMA array and we will try to obtain the real ring of Sgr A*.

Lastly, we are examining the effects of scattering on hotspot tracking, which could provide deeper insights into the complex dynamics of the system.

8. Summary and Conclusions

Scattering remains one of the most significant challenges in radio astronomical observations of the Galactic Plane, particularly at low frequencies. It complicates image reconstruction by introducing substantial stochastic distortions that can severely degrade the quality of recovered images (Johnson & Narayan 2016) and corrupt signals posing considerable difficulties for tasks such as pulsar searches (Narayan 1992).

Several methods have been developed to mitigate its effects (Fish et al. 2014; Johnson et al. 2018) and even to reconstruct the affecting screen. However, these methods are constrained by their tendency to find only local minima and are limited to a restricted set of regularizers due to computational power constraints.

In this work, we have introduced a new scattering mitigation and screen reconstruction strategy that integrates the modeling of Stochastic Optics within a multiobjective optimization framework. Our method provides a mathematically rigorous solution to the problem without being restricted to a specific screen model or intrinsic source structure. This flexibility is particularly valuable for tackling the highly non-linear and ill-posed nature of VLBI imaging and screen modeling. In contrast to traditional noise-inflation and deblurring techniques (Event Horizon Telescope Collaboration et al. 2022c, 2024a), as well as standard unimodal exploration (Johnson 2016), our strategy thoroughly explores the family of local solutions, a crucial aspect often overlooked in conventional approaches. In this way, this approach solves the challenges faced by previous methods, such as: 1) high computational cost, 2) inefficiency due to the increased dimensionality of the problem by the inclusion of a new regularizer, and 3) loss of information about the effects of scattering mitigation on the image. By solving Problem (MOP Scalar) using nature-inspired optimization techniques—specifically genetic algorithms and particle swarm optimization—we have effectively explored the problem's multimodal nature.

We have demonstrated how this novel strategy successfully mitigates scattering in very sparse EHT observations of approximately 100 minutes at 230 GHz, where scattering noise is weak and poorly constrained, and in high SNR GMVA+ALMA observations at 86 GHz, lasting about 12 hours, where scattering is stronger and better constrained.

We have applied our algorithm to synthetic EHT observations, testing various screen velocities, intrinsic geometric sources, levels of gain corruption, and different priors. In all cases, the recovered unscattered source and the corrupting scattering screens were well reconstructed. Notably,

even under these poorly constrained conditions, our method succeeded in recovering the screen’s velocity—an improvement over earlier approaches, and crucial for constraining the expected range (Gwinn et al. 1991; Reid et al. 2019). However, in this high-frequency domain, the prior screen proved crucial for aiding convergence, as expected due to the poorly constrained nature of the problem.

Additionally, we have modeled a ring structure and applied the scattering kernel predicted by Bower et al. (2015); Psaltis et al. (2018) for Sgr A* at 86 GHz, introducing various gain corruptions and consistently assuming adverse weather conditions. Our objective was to recover the intrinsic ring structure despite these challenges. Leveraging the significant exploration capabilities of Genetic Algorithms, we have been able to successfully reconstruct both the intrinsic ring and the scattering screen.

To this end, we have proposed two different strategies based on the level of gain corruptions under two representative gain corruption conditions. While one is designed to explore multimodality only, the second one, selects the most probable solution and self-calibrates to it, iterating this procedure as many times as the user imposes.

We have analyzed the different local minima we have recovered and determined which many of them had a ring morphology based on different initial configurations (Gaussian, ring, and disk). Our findings indicate that, for instance, starting from a disk configuration presents the highest likelihood of failure in accurately recovering the ring. Because of the more constrained nature of this problem, we have been able to recover a better image of the scattering screen.

Lastly, we explored the marginal contribution of the Stochastic Optics regularizer. Our findings confirm that at lower frequencies, where long baselines are dominated by refractive noise, the constraints are tighter, reducing the regularizer’s degrees of freedom.

In conclusion, multiobjective optimization together with exploration algorithms is a tool that could potentially enhance our ability to see the ring of Sgr A* in real GMVA+ALMA observations at 86 GHz, a frequency at which it has not yet been detected.

Acknowledgements. This work was supported by the Italian Ministry of University and Research (MUR)– Project CUP F53D23001260001, funded by the European Union – NextGenerationEU. T.T. acknowledge the “Center of Excellence Severo Ochoa” grant CEX2021-001131-S funded by MCIN/AEI/ 10.13039/501100011033 awarded to the Instituto de Astrofísica de Andalucía. H.M, G.Y and A.L. acknowledge the M2FINDERS project funded by the European Research Council (ERC) under the European Union’s Horizon 2020 Research and Innovation Programme (Grant Agreement No. 101018682) and by the MICINN Research Project PID2019-108995GB-C22. The National Radio Astronomy Observatory is a facility of the National Science Foundation operated under cooperative agreement by Associated Universities, Inc. The authors gratefully acknowledge Y. Kovalev for his insightful comments and valuable suggestions, and the anonymous referee for their constructive feedback.

Software Availability Our imaging pipeline and our software is included in the second release of MrBeam ⁶. Our software makes use of the publicly available eht-imaging library (Chael et al. 2016, 2018), regpy (Regpy 2019), MrBeam (Müller & Lobanov 2022, 2023b,a; Müller et al. 2023) and pyswarms ⁷ packages.

References

- Akiyama, K., Ikeda, S., Pleau, M., et al. 2017a, *AJ*, 153, 159
Akiyama, K., Kuramochi, K., Ikeda, S., et al. 2017b, *ApJ*, 838, 1
Beniamini, P., Wadiasingh, Z., Hare, J., et al. 2023, *MNRAS*, 520, 1872
Blandford, R. & Narayan, R. 1985, *MNRAS*, 213, 591
Born, M. & Wolf, E. 1980, *Principles of Optics Electromagnetic Theory of Propagation, Interference and Diffraction of Light*
Bouman, K. L., Johnson, M. D., Dalca, A. V., et al. 2017, *arXiv e-prints*, arXiv:1711.01357
Bower, G. C., Deller, A., Demorest, P., et al. 2014, *ApJ*, 780, L2
Bower, G. C., Falcke, H., Herrnstein, R. M., et al. 2004, *Science*, 304, 704
Bower, G. C., Markoff, S., Dexter, J., et al. 2015, *ApJ*, 802, 69
Broderick, A. E., Gold, R., Karami, M., et al. 2020, *ApJ*, 897, 139
Caleb, M., Heywood, I., Rajwade, K., et al. 2022, *Nature Astronomy*, 6, 828
Chael, A. A., Johnson, M. D., Bouman, K. L., et al. 2018, *ApJ*, 857, 23
Chael, A. A., Johnson, M. D., Narayan, R., et al. 2016, *ApJ*, 829, 11
Chavez, E., Issaoun, S., Johnson, M. D., et al. 2024, *arXiv e-prints*, arXiv:2405.06029
Clark, B. G. 1980, *A&A*, 89, 377
Cordes, J. M. & Lazio, T. J. W. 2002, *arXiv e-prints*, astro
Cornwell, T. J. 2008, *IEEE Journal of Selected Topics in Signal Processing*, 2, 793
Dexter, J., Deller, A., Bower, G. C., et al. 2017, *MNRAS*, 471, 3563
Du, K.-L. & Swamy, M. N. S. 2016, *Search and Optimization by Metaheuristics: Techniques and Algorithms Inspired by Nature*, 1st edn. (Birkhäuser Basel)
Event Horizon Telescope. 2025, manuscript in preparation
Event Horizon Telescope Collaboration, Akiyama, K., Alberdi, A., et al. 2024a, *ApJ*, 964, L25
Event Horizon Telescope Collaboration, Akiyama, K., Alberdi, A., et al. 2024b, *ApJ*, 964, L26
Event Horizon Telescope Collaboration, Akiyama, K., Alberdi, A., et al. 2024c, *A&A*, 681, A79
Event Horizon Telescope Collaboration, Akiyama, K., Alberdi, A., et al. 2023, *ApJ*, 957, L20
Event Horizon Telescope Collaboration, Akiyama, K., Alberdi, A., et al. 2022a, *ApJ*, 930, L12
Event Horizon Telescope Collaboration, Akiyama, K., Alberdi, A., et al. 2022b, *ApJ*, 930, L13
Event Horizon Telescope Collaboration, Akiyama, K., Alberdi, A., et al. 2022c, *ApJ*, 930, L14
Event Horizon Telescope Collaboration, Akiyama, K., Alberdi, A., et al. 2022d, *ApJ*, 930, L15
Event Horizon Telescope Collaboration, Akiyama, K., Alberdi, A., et al. 2022e, *ApJ*, 930, L16
Event Horizon Telescope Collaboration, Akiyama, K., Alberdi, A., et al. 2022f, *ApJ*, 930, L17
Event Horizon Telescope Collaboration, Akiyama, K., Alberdi, A., et al. 2019a, *ApJ*, 875, L2
Event Horizon Telescope Collaboration, Akiyama, K., Alberdi, A., et al. 2019b, *ApJ*, 875, L1
Event Horizon Telescope Collaboration, Akiyama, K., Alberdi, A., et al. 2019c, *ApJ*, 875, L3
Event Horizon Telescope Collaboration, Akiyama, K., Alberdi, A., et al. 2019d, *ApJ*, 875, L4
Event Horizon Telescope Collaboration, Akiyama, K., Alberdi, A., et al. 2019e, *ApJ*, 875, L5
Event Horizon Telescope Collaboration, Akiyama, K., Alberdi, A., et al. 2019f, *ApJ*, 875, L6
Event Horizon Telescope Collaboration, Akiyama, K., Alberdi, A., et al. 2021a, *ApJL*, 910, 48
Event Horizon Telescope Collaboration, Akiyama, K., Alberdi, A., et al. 2021b, *ApJL*, 910, 43
Farah, J., Galison, P., Akiyama, K., et al. 2022, *The Astrophysical Journal Letters*, 930, 1
Fish, V. L., Johnson, M. D., Lu, R.-S., et al. 2014, *ApJ*, 795, 134
Goddi, C., Falcke, H., Kramer, M., et al. 2017, *International Journal of Modern Physics D*, 26, 1730001
Goodman, J. & Narayan, R. 1989, *MNRAS*, 238, 995
Gwinn, C. R., Danen, R. M., Middleditch, J., Ozernoy, L. M., & Tran, T. K. 1991, *ApJ*, 381, L43
Högbom, J. A. 1974, *A&AS*, 15, 417
Issaoun, S., Johnson, M. D., Blackburn, L., et al. 2019, *ApJ*, 871, 30
Johnson, M. D. 2016, *ApJ*, 833, 74

⁶ <https://github.com/hmuellergoe/mrbeam>

⁷ <https://pyswarms.readthedocs.io/en/latest/>

- Johnson, M. D., Bouman, K. L., Blackburn, L., et al. 2017, ApJ, 850, 172
- Johnson, M. D. & Gwinn, C. R. 2015, ApJ, 805, 180
- Johnson, M. D. & Narayan, R. 2016, ApJ, 826, 170
- Johnson, M. D., Narayan, R., Psaltis, D., et al. 2018, ApJ, 865, 104
- Jonson, B. 1999, in American Institute of Physics Conference Series, Vol. 495, Experimental Nuclear Physics in europe: Facing the next millennium (AIP), 3–8
- Kim, J.-S., Mueller, H., Nikonov, A. S., et al. 2024a, arXiv e-prints, arXiv:2409.00540
- Kim, J.-S., Nikonov, A. S., Roth, J., et al. 2024b, arXiv e-prints, arXiv:2407.14873
- Kouroshnia, A., Nguyen, K., Ni, C., SaraerToosi, A., & Broderick, A. E. 2025, arXiv preprint arXiv:2501.14055, submitted to ApJ
- Li, H. & Zhang, Q. 2009, IEEE Transactions on Evolutionary Computation, 13, 284
- Little, L. T. 1973, Astrophys. Lett., 13, 115
- Litvak, M. M. 1971, ApJ, 170, 71
- Lu, R.-S., Asada, K., Krichbaum, T. P., et al. 2023, Nature, 616, 686
- Mościbrodzka, M., Falcke, H., & Shiokawa, H. 2016, A&A, 586, A38
- Mościbrodzka, M., Falcke, H., Shiokawa, H., & Gammie, C. F. 2014, A&A, 570, A7
- Müller, H. 2024, A&A, 689, A299
- Müller, H. & Lobanov, A. P. 2022, A&A, 666, A137
- Müller, H. & Lobanov, A. P. 2023a, A&A, 673, A151
- Müller, H. & Lobanov, A. P. 2023b, A&A, 672, A26
- Müller, H., Massa, P., Mus, A., Kim, J.-S., & Perracchione, E. 2024, A&A, 684, A47
- Müller, H., Mus, A., & Lobanov, A. 2023, A&A, 675, A60
- Mus, A. & Martí-Vidal, I. 2024, Monthly Notices of the Royal Astronomical Society, stae234
- Mus, A., Müller, H., & Lobanov, A. 2024a, A&A, 688, A100
- Mus, A., Müller, H., Martí-Vidal, I., & Lobanov, A. 2024b, A&A, 684, A55
- Narayan, R. 1992, Philosophical Transactions of the Royal Society of London Series A, 341, 151
- Narayan, R. & Goodman, J. 1989, MNRAS, 238, 963
- Pardalos, P. M., Žilinskas, A., & Žilinskas, J. 2017, Non-Convex Multi-Objective Optimization
- Pesce, D. 2022, ngehtsim Documentation, <https://smithsonian.github.io/ngehtsim/html/docs/source/index.html>
- Psaltis, D., Johnson, M., Narayan, R., et al. 2018, arXiv e-prints, arXiv:1805.01242
- Raymond, A. W., Doeleman, S. S., Asada, K., et al. 2024, AJ, 168, 130
- Raymond, A. W., Palumbo, D., Paine, S. N., et al. 2021, ApJS, 253, 5
- Regpy. 2019, "regpy: Python tools for regularization methods", <https://github.com/regpy/regpy>
- Reid, M. J., Menten, K. M., Brunthaler, A., et al. 2019, ApJ, 885, 131
- Richstone, D., Ajhar, E. A., Bender, R., et al. 1998, Nature, 385, A14
- Rickett, B. J. 1990, ARA&A, 28, 561
- Roelofs, F., Blackburn, L., Lindahl, G., et al. 2023, Galaxies, 11, 12
- Taylor, J. H. & Cordes, J. M. 1993, ApJ, 411, 674
- Thompson, A. R., Moran, J. M., & Swenson, George W., J. 2017, Interferometry and Synthesis in Radio Astronomy, 3rd Edition
- Tiede, P. 2022, The Journal of Open Source Software, 7, 4457
- Wielgus, M., Marchili, N., Martí-Vidal, I., et al. 2022, ApJ, 930, L19
- Wiener, N. 1949, Extrapolation, Interpolation, and Smoothing of Stationary Time Series: With Engineering Applications (The MIT Press)
- Zhang, Q. & Li, H. 2007, IEEE Transactions on Evolutionary Computation, 11, 712

Appendix A: Additional Figures

Appendix B: Pareto fronts

In this appendix we show the Pareto fronts of the different sources discussed in the main text.

Appendix C: Comparison metrics

In this section, we present the **nxcorr** values obtained from all the reconstructions performed. Table C.1 contains the **nxcorr** values of the reconstructions of the intrinsic descattered source and the recovered (blurred and non-blurred) scattering screen appearing in Figures 2, 3 and 7. It is important to note that the **nxcorr** tends to improve at lower frequencies, which is an expected outcome due to the increased constraints at those frequencies. However, it should also be noted that the **nxcorr** may not be the most suitable metric for evaluation. The **nxcorr** assumes a Pearson correlation, which may not be optimal for non-normally distributed data and because of the given the high variance in pixel brightness values (ranging between -3000 to 3000 radians in some instances), which significantly reduces the accuracy of the comparisons.

$$\rho_{\text{NX}}(X, Y) = \frac{1}{N} \sum_i \frac{(X_i - \langle X \rangle)(Y_i - \langle Y \rangle)}{\sigma_X \sigma_Y}. \quad (\text{C.1})$$

Eq. (C.1) provides the definition of **nxcorr**, used to compare two images, X and Y . Due to the high variance in this context, the application of the mean and normalization by the standard deviation (σ) may be less appropriate. As discussed in Sect. 7, we are developing a more sophisticated metric to address these limitations.

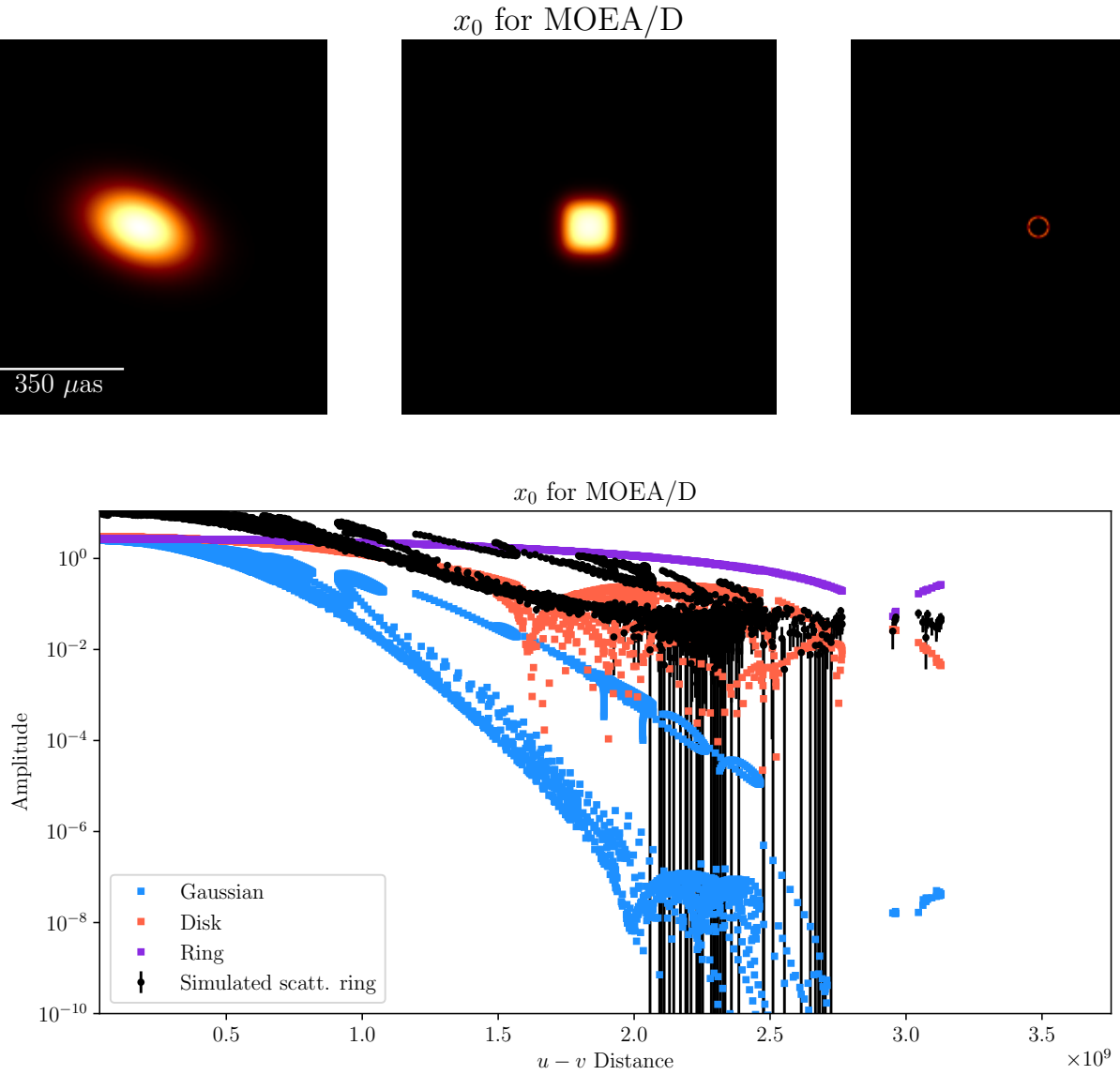


Fig. A.1: To explore the multimodality of the solutions at 86 GHz we set the starting point for MOEA/D to be a Gaussian (corresponding to LSQ solution in Issaoun et al. 2019), disk and ring. Top row of the figure shows the images, bottom row, the amplitude vs uv-distance including the simulated scattered ring (black dots).

Table C.1: **nxcorr** values for the different reconstructions presented.

	nxcorr intrinsic source	nxcorr blurred screen	nxcorr non-blurred screen
Figure 2	0.99 (top row); 0.99 (bottom row)	0.55 (top row); 0.57 (bottom row)	0.73 (top row); 0.75 (bottom row)
Figure 3	0.99 (top row); 0.99 (bottom row)	0.57 (top row); 0.45 (bottom row)	0.75 (top row); 0.55 (bottom row)
Figure 7	0.97	0.81	0.88

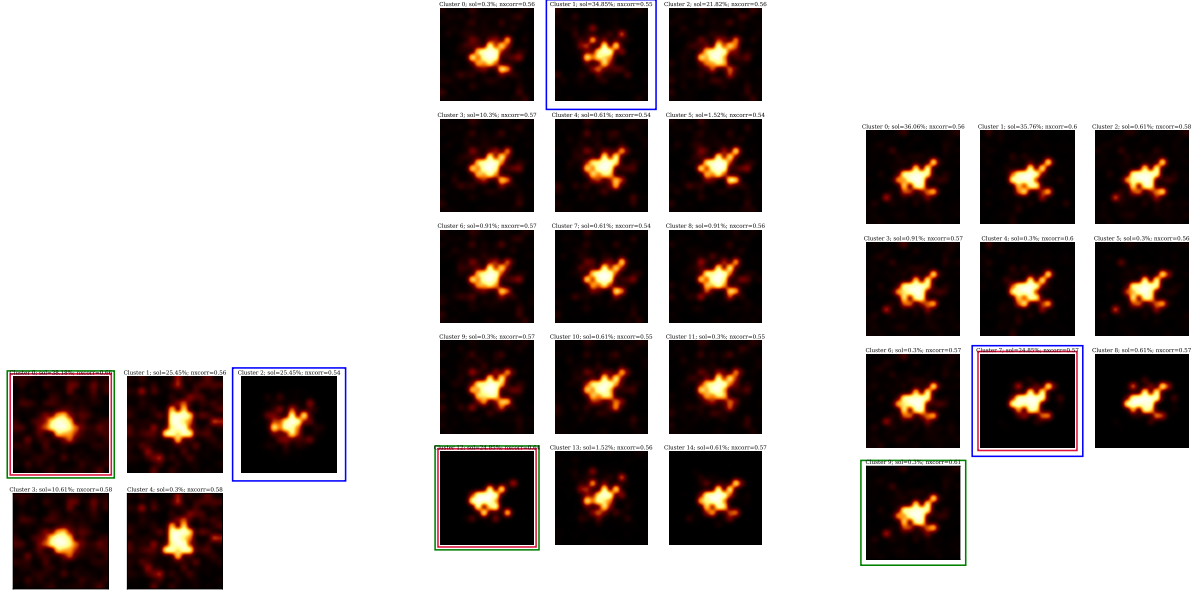


Fig. B.1: Pareto front for the intrinsic source at 86 GHz across each self-calibration iteration. Arranged from left to right, the panels correspond to the first, second, and third iterations, respectively. In the initial iteration, the ring structure is absent from the solution set. A hint of the ring appears in the second iteration, meaning the null in the visibilities is presented in the set of local minima. In addition, we note how the diversity of solutions increases. The red box encapsulates the most frequently repeated (most probable) solution, the blue box highlights the solution closest to the ideal, and the green box identifies the one with the lowest χ^2 .

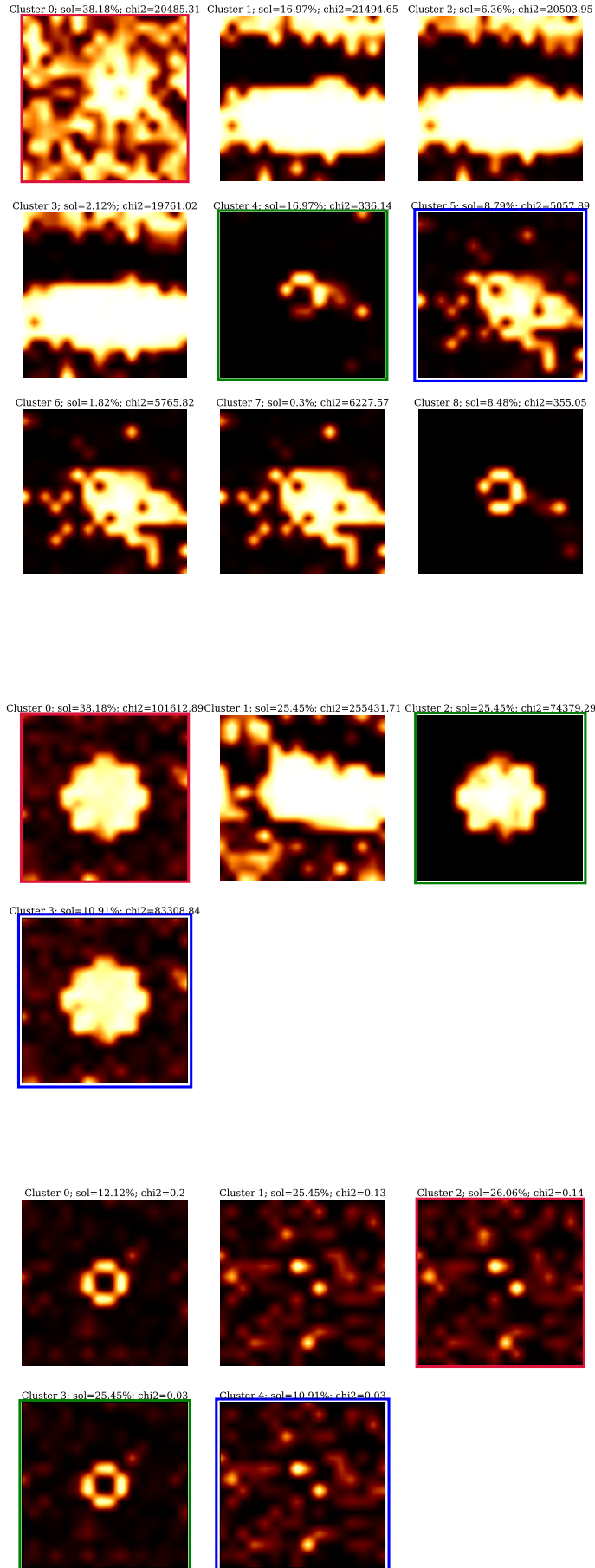


Fig. B.2: Pareto front for the intrinsic source at 86 GHz. The top set of images corresponds to the Gaussian (LSQ Issaoun et al. 2019) starting point, the second set to a disk, and the third to a ring. The red box encapsulates the most frequently repeated (most probable) solution, the blue box highlights the solution closest to the ideal, and the green box identifies the one with the lowest χ^2 .